UC Berkeley

UC Berkeley Previously Published Works

Title

Biporous Metal-Organic Framework with Tunable CO_2/CH_4 Separation Performance Facilitated by Intrinsic Flexibility.

Permalink

https://escholarship.org/uc/item/60j1m00v

Journal

ACS applied materials & interfaces, 10(42)

ISSN

1944-8244

Authors

Gładysiak, Andrzej
Deeg, Kathryn S
Dovgaliuk, Iurii
et al.

Publication Date

2018-10-01

DOI

10.1021/acsami.8b13362

Peer reviewed

eScholarship.org Powered by the California Digital Library
University of California

This is an open access article published under an ACS AuthorChoice License, which permits copying and redistribution of the article or any adaptations for non-commercial purposes.

ACS APPLIED MATERIALS & INTERFACES

Research Article

Cite This: ACS Appl. Mater. Interfaces 2018, 10, 36144−36156

www.acsami.org

Biporous Metal−Organic Framework with Tunable CO_2/CH_4 Separation Performance Facilitated by Intrinsic Flexibility

Andrzej Gładysiak,[†] Kathryn S. Deeg,[‡] Iurii Dovgaliuk,[§] Arunraj Chidambaram,[†] Kaili Ordiz,[∥] Peter G. Boyd,[†] Seyed Mohamad Moosavi,[†] Daniele Ongari,[†] Jorge A. R. Navarro,[⊥] Berend Smit,[†,‡,∥] and Kyriakos C. Stylianou*[,†]

[†]Laboratory of Molecular Simulation (LSMO), Institut des sciences et ingénierie chimiques (ISIC), École polytechnique fédérale de Lausanne (EPFL) Valais, Rue de l'Industrie 17, 1951 Sion, Switzerland

[‡]Department of Chemistry, University of California, Berkeley, California 94720, United States

[§]Swiss-Norwegian Beamlines, European Synchrotron Radiation Facility, 38000 Grenoble, France

[∥]Department of Chemical and Biomolecular Engineering, University of California, Berkeley, California 94720, United States

[⊥]Departamento de Química Inorgánica, Universidad de Granada, Av. Fuentenueva S/N, 18071 Granada, Spain

Supporting Information

ABSTRACT: In this work, we report the synthesis of **SION-8**, a novel metal−organic framework (MOF) based on Ca(II) and a tetracarboxylate ligand $TBAPy^{4-}$ endowed with two chemically distinct types of pores characterized by their hydrophobic and hydrophilic properties. By altering the activation conditions, we gained access to two bulk materials: the fully activated **SION-8F** and the partially activated **SION-8P** with exclusively the hydrophobic pores activated. **SION-8P** shows high affinity for both CO_2 (Q_{st} = 28.4 kJ/mol) and CH_4 (Q_{st} = 21.4 kJ/mol), while upon full activation, the difference in affinity for CO_2 (Q_{st} = 23.4 kJ/mol) and CH_4 (Q_{st} = 16.0 kJ/mol) is more pronounced. The intrinsic flexibility of both materials results in complex adsorption behavior and greater adsorption of gas molecules than if the materials were rigid. Their CO_2/CH_4 separation performance was tested in fixed-bed breakthrough experiments using binary gas mixtures of different compositions and rationalized in terms of molecular interactions. **SION-8F** showed a 40−160% increase (depending on the temperature and the gas mixture composition probed) of the CO_2/CH_4 dynamic breakthrough selectivity compared to **SION-8P**, demonstrating the possibility to rationally tune the separation performance of a single MOF by manipulating the stepwise activation made possible by the MOF's biporous nature.

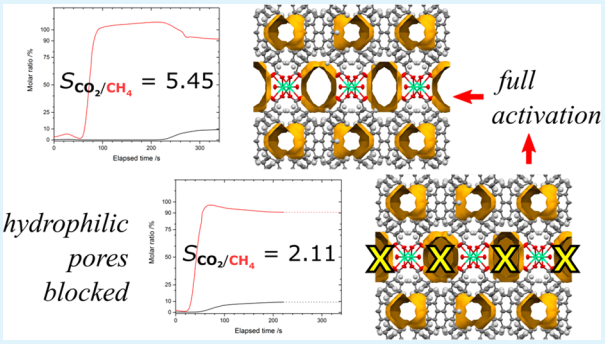

KEYWORDS: *metal−organic frameworks, biporous MOFs, gas adsorption, breakthrough curves, CO_2/CH_4 separation*

INTRODUCTION

Efficient gas mixture separations are a continued challenge for the modern chemical industry. While classical separation techniques, including cryogenic distillation and low-temperature chemical absorption in aqueous alcoholamine and glycol derivatives solutions, are widely in use, they are energetically costly and present environmental issues, primarily due to the thermal solvent degradation and possible NO_x emission.[1] Among different solutions being developed as alternatives to these techniques, pressure swing adsorption using a range of porous adsorbents, characterized by lower investment costs and lower complexity, is showing great promise.[2]

The removal of CO_2 from gas streams containing primarily CH_4 is one of the most important gas separation processes worldwide. Natural gas, an important fuel and chemical raw material, contains variable amounts of CO_2, typically 5−15%, but in some wells, its content may reach 40%.[3] This percentage is normally higher in biogas, a mixture of gases produced by anaerobic fermentation of organic wastes (when these wastes originate from landfill deposits, the term "landfill gas" is used) and can reach 30−40%.[4] Removal of CO_2 from these gases is necessary to meet both technological (lowering the risk of pipeline corrosion) and economic (raising the value of the gas being transported) standards.[5] Nevertheless, engineering porous materials for CO_2/CH_4 separation is challenging due to the close similarity of these two molecules. They are both characterized by zero dipole moment, and their kinetic diameters (CO_2: 3.3 Å; CH_4: 3.8 Å)[6] and polarizabilities (CO_2: 2.63 × 10^{-40} $J^{-1}\cdot C^2\cdot m^2$; CH_4: 2.60 × 10^{-40} $J^{-1}\cdot C^2\cdot m^2$)[7] are comparable. Indeed, their quadrupole moments make the

Received: August 5, 2018
Accepted: September 24, 2018
Published: September 24, 2018

© 2018 American Chemical Society

DOI: 10.1021/acsami.8b13362
ACS Appl. Mater. Interfaces 2018, 10, 36144−36156

only appreciable difference between CO_2 (q_{CO_2} = 13.4 × 10^{-40} C·m^2) and CH_4 (q_{CH_4} = 0)[6] in terms of physical properties. This is the reason why chemical interactions between the pore surface and an adsorbate are by far more exploited in separation processes. CO_2 is an inorganic acid anhydride, and its lone electron pairs are known to interact with open metal sites,[8,9] negatively charged species,[10] and amines adsorbed on metal−organic framework (MOF) surfaces.[11,12] On the other hand, CH_4 is chemically inert and interacts with adsorbents only through weak dispersion interactions.[13]

Metal−organic frameworks (MOFs) are porous crystalline materials constructed from the self-assembly of organic ligands linked together by inorganic metal centers, and have shown great potential in many applications including gas adsorption,[14,15] sensing,[16,17] and removal of toxic species.[18−21] Capitalizing on modular synthesis routes of MOFs and their structural tunability and possibility of pore functionalization, many MOFs have been shown to efficiently separate gas mixtures. Biporous MOFs, in particular, have been shown to exhibit interesting behavior especially for gas separations,[22] while biporous coordination networks have been studied for their interesting behavior for separations[23] and storage of differing species.[24,25] Such MOFs, only a handful of which have been reported, offer different chemical environments within a single material, leading to complex and varied structure−adsorbate chemical interactions that can be harnessed for gas separations and other applications. Thus, we emphasize the importance of fully understanding and characterizing such materials, as we have undertaken for the MOF introduced here.

In this account, we present the synthesis of a novel biporous MOF based on Ca(II) and a tetracarboxylate ligand $TBAPy^{4-}$ (Scheme 1) featuring two chemically distinct types of pores:

Scheme 1. Structural Formula of H_4TBAPy

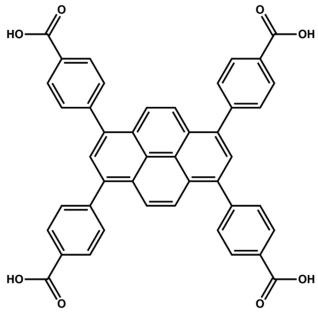

hydrophobic and hydrophilic. Owing to judicious choice of conditions, we gained access to both the fully activated material and the partially activated material with exclusively hydrophobic pores activated. The difference of the sorption behavior of these materials was rationalized in terms of different molecular interactions between the partially or the fully activated material and CO_2 or CH_4, and the selectivity of CO_2 over CH_4 was studied with breakthrough experiments and molecular simulations.

EXPERIMENTAL SECTION

Synthesis of SION-8. The ligand, 1,3,6,8-tetrakis(*p*-benzoic acid)pyrene (H_4TBAPy), was synthesized using the procedure reported elsewhere.[26] The reaction between 10 mg (0.0680 mmol) of $CaCl_2·2H_2O$ and 10 mg (0.0146 mmol) of H_4TBAPy in the solution composed of 2 mL of *N*,*N*-dimethylformamide (DMF), 1 mL of H_2O, and 80 μL of HCl (techn., 32%) at 393 K for 72 h resulted in 11.85 mg (0.0126 mmol, 86.0% yield) of $[Ca_2(TBAPy)(\mu_2\text{-}OH_2)_2]·2DMF$ in the form of yellow block-shaped crystals suitable for single-crystal X-ray diffraction (SCXRD) analysis.

SCXRD Analysis. The crystals were analyzed with monochromatic synchrotron radiation on the single-crystal diffractometer equipped with a Pilatus2M 2-dimensional CCD detector at the BM01 Beamline of the ESRF.[27] The crystal structure was solved with SHELXT[28] and refined with SHELXL[29] programs implemented in the Olex2 program suite.[30] Structure simplification and net classification were performed using the TOPOS Pro program suite.[31] Volume and electron count of the structural voids were calculated with the SQUEEZE procedure of the PLATON program suite;[32] the excess electron density was further interpreted in terms of number of DMF molecules based on the number of electrons of a DMF molecule (C_3H_7NO, 40 e^-). The same program was also used to calculate the crystal-derived pore volume.

In an *in situ* SCXRD experiment, a single crystal of **SION-8** was stuck onto the top of the glass fiber and enclosed in an environment cell constructed upon a sealed glass capillary connected to the pressure control system. The experimental setup was complemented with a temperature attachment allowing for flexible changes of temperature.

(a) During the stepwise activation experiment, vacuum, as low as 10^{-3} mbar, was achieved using a molecular vacuum pump. At each temperature point in the 300−400 K range, the diffraction data were collected, which allowed for the structure solution and further refinement.

(b) During the variable-pressure (VP) experiments, increasingly higher pressures of N_2 (0−6000 mbar), CO_2 (0−14 000 mbar), and CH_4 (0−5000 mbar) were exerted on a studied single crystal. Constant temperature was maintained (90 K for N_2 and 300 K for CO_2 and CH_4), while the pressure was changed before each data collection point. Excess electron density found in the refined structures was interpreted in terms of number of gas molecules based on their electron counts (N_2: 14 e^-; CO_2: 20 e^-; CH_4: 10 e^-).

VT and VP PXRD Analysis and Complementary Bulk Characterization. Powder X-ray diffraction (PXRD) patterns were recorded using synchrotron radiation at BM01 and BM31 from SNBL (ESRF in Grenoble, France). The samples were packed into glass capillaries, and the PXRD patterns were measured at temperatures controlled with a Cryostream 700+ nitrogen blower. In the variable-temperature (VT) PXRD experiment (λ = 0.75190 Å) bulk powder of as-synthesized **SION-8** was heated at a rate of 5 K/min from 100 to 500 K. In the VP PXRD experiment, the glass capillary was filled with **SION-8F** and attached to the gas system described above for a single-crystal experiment. Le Bail fits were performed with the FullProf program suite,[33] wherein the unit-cell parameters were refined in the space group *Pbam*.

Complementary infrared (IR) spectra were collected on a Perkin Elmer FT-IR/FIR Frontier Spectrometer. Thermogravimetric analysis (TGA) was performed on a sample heated at a constant rate of 5 K/min with air acting as carrier gas.

Sorption Studies. Gravimetric gas sorption measurements were performed using the Intelligent Gravimetric Analyzer Instrument (IGA) from Hiden. Values of Q_{st} at zero loading were calculated from Henry's constants derived from the single-component adsorption isotherms recorded at different temperatures following a method published previously.[34]

Breakthrough Experiments. In a typical experiment, the **SION-8P** or **SION-8F** bulk powder was packed into a stainless steel column characterized by the length of 12 cm and internal diameter of 0.5 cm. Following the *in situ* activation under the constant flow of helium, the fixed bed of the material was subjected to one of the CO_2/CH_4 gas mixtures at 1 bar and at a constant flow of 10 mL/min. Relative molar ratios of gases passing through the fixed bed were achieved with mass flow controllers, and the column was thermostated at a desired temperature. Composition of the outlet gas mixture was monitored

DOI: 10.1021/acsami.8b13362
ACS Appl. Mater. Interfaces 2018, 10, 36144−36156

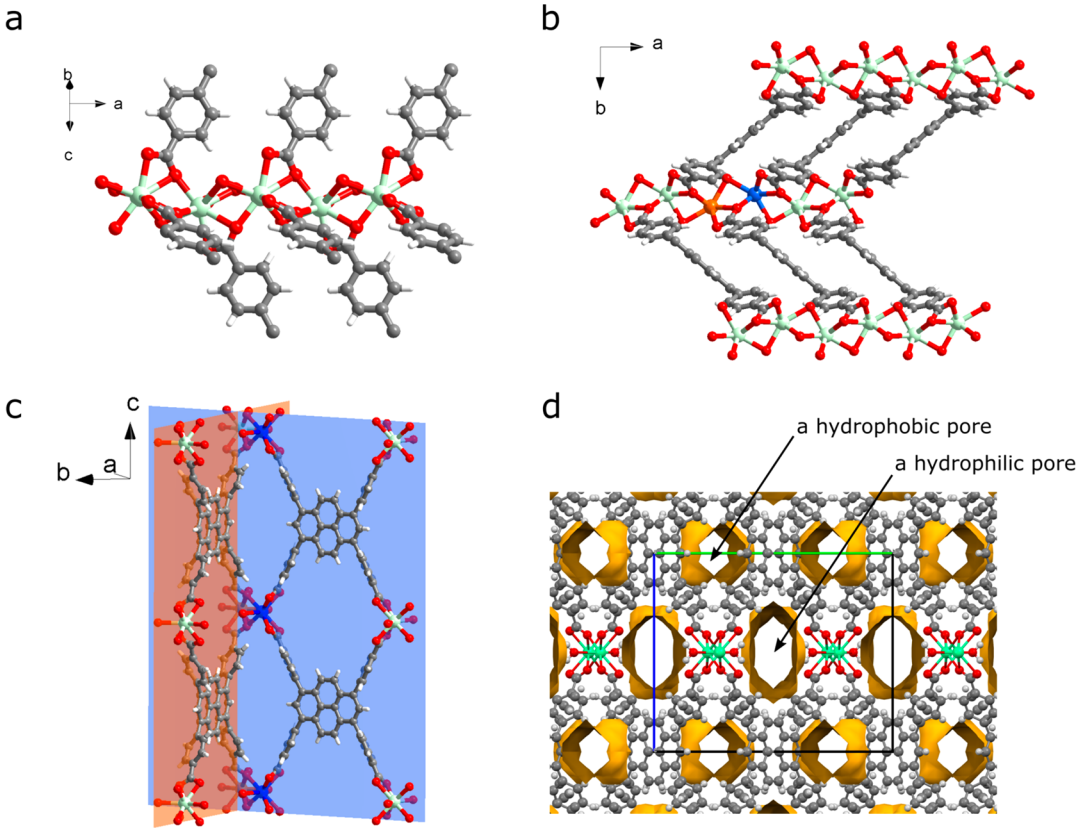

Figure 1. (a) A chain of alternating Ca−O atoms running along [100]. (b) Arrangement of the $TBAPy^{4-}$ ligands relative to the Ca−O chains. View along [001] features the close packing. Two consecutive Ca atoms are marked in blue and orange. (c) A dihedral angle between the planes of $TBAPy^{4-}$ ligands bound to two subsequent Ca atoms (marked in blue and orange) of 80.06°. (d) Tubular structural voids extending along the [100] direction, marked as gold surfaces, occupying 24.8% of the unit-cell volume. The unit-cell contour, with *b* and *c* edges colored in green and blue, respectively, is outlined. Color code: C, gray; H, white; O, red; Ca, light green.

with a Mass Spectrometer Gas Analysis System. A regeneration procedure was carried out before each new experiment. Adsorption capacities of **SION-8P** and **SION-8F** were calculated by integrating breakthrough curves following the procedure reported elsewhere.[35−37] Dynamic breakthrough selectivities, α, were calculated using the expression $\alpha = (q_{CO_2}/q_{CH_4})/(x_{CO_2}/x_{CH_4})$, where q = adsorption capacity (mmol/g) and x = molar ratio, reported elsewhere.[14]

COMPUTATIONAL METHODS

Periodic Density Functional Theory. Structure relaxation and binding energy calculations were performed using periodic density functional theory (DFT) calculations as implemented in the Quantum Espresso software package.[38] The PBE functional[39] as well as the DFT-D2 correction for dispersion interactions[40] were used for all calculations. The projector-augmented wave approximation (PAW)[41] was adopted, using a plane-wave kinetic energy cutoff of 90 Ry, which ensures the electron energy is converged to within 1 mRy. The Brillouin-zone sampling was performed on a Gamma-centered Monkhorst−Pack *k*-point mesh of 2 × 1 × 1 points, due to the unit cell's short *a*-dimension (about 7 Å).

The crystal structure used in all simulations was obtained by performing a DFT relaxation on the experimentally determined structure.

Binding energies (BE) for an adsorbate (ads) were computed according to the following formula.

$$\mathrm{BE(ads)} = E(\mathrm{MOF + ads}) - E(\mathrm{MOF}) - E(\mathrm{ads})$$

For DMF binding energies, E(MOF + ads) was computed by allowing the DMF molecule as well as the MOF atom positions and unit-cell dimensions to change during the DFT relaxation. We found that assuming a nonrigid MOF was necessary to capture the hydrogen bonding that occurs between a DMF molecule and a bound water molecule in the hydrophilic pore.

Monte Carlo. CH_4, CO_2, and N_2 adsorption isotherms were computed using grand canonical Monte Carlo (GCMC) simulations performed in the RASPA software package.[42] Lennard-Jones potentials were truncated and shifted to zero at 12 Å. Coulombic interactions were computed using the Ewald summation method. CO_2, CH_4, and N_2 molecules were modeled using the TraPPE force field.[43,44] DMF Lennard-Jones parameters were those presented by Sarkisov,[45] with the charges presented by Vasudevan and Mushrif.[46] MOF Lennard-Jones parameters were taken from Wu et al.;[47] we adopted this force field because it was developed for ZIF-8, a small-pore MOF, as is **SION-8**. Framework oxygen Lennard-Jones parameters were obtained using the formula described by Wu et al.,[47] for modifying UFF parameters. MOF atom charges were computed using the REPEAT scheme.[48] Lorentz−Berthelot mixing rules were applied to all heterogeneous Lennard-Jones parameters. At least 10^5 (CH_4) and 5×10^4 (CO_2) equilibration cycles of Monte Carlo trial moves and 2.5×10^5 (CH_4) and 1.2×10^5 (CO_2) production cycles were performed in each simulation. Adsorption isotherms in **SION-8P** were obtained by placing noninteracting blocking spheres in the hydrophilic pores. Heats of adsorption at nonzero loading were computed from GCMC simulations based on energy/particle fluctuations, while those at zero loading were computed using Widom insertions.[49]

Probability density plots of adsorbate positions of CO_2 and CH_4 in **SION-8** were generated from NVT simulations, using the force fields described above. 10^5 initialization cycles were performed for each simulation, and adsorbate positions were recorded every 10 or more production cycles such that positions of at least 6×10^6 individual adsorbate molecules were recorded. The plots were generated using a

DOI: 10.1021/acsami.8b13362
ACS Appl. Mater. Interfaces 2018, 10, 36144−36156

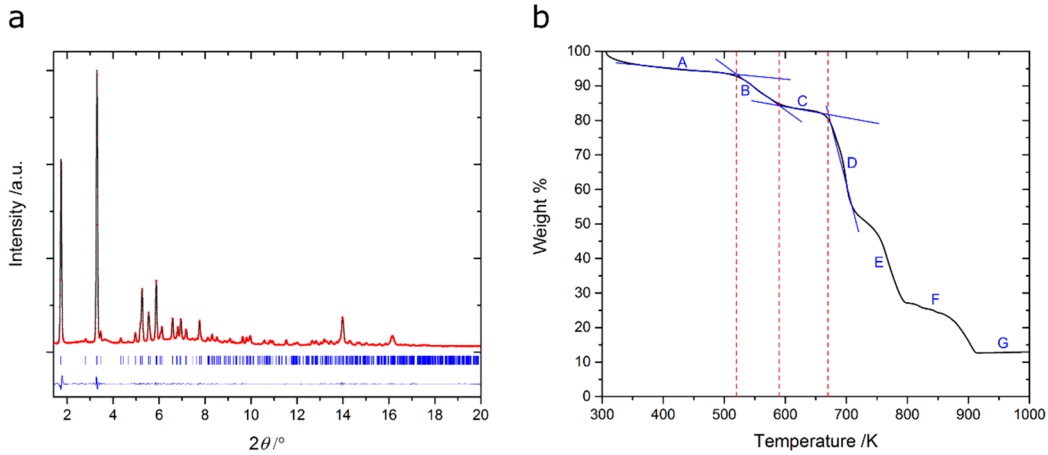

Figure 2. (a) PXRD Le Bail refinement of **SION-8** (space group *Pbam*: R_p = 3.65%, R_{wp} = 3.41%, a = 6.92670(9) Å, b = 20.415(3) Å, c = 16.572(2) Å; λ = 0.50084 Å). The black plots represent the experimental data, and the red dots show the refined Le Bail profiles, while the blue plots represent the difference between them. Reflection positions are marked in blue. (b) Thermogravimetric analysis of **SION-8**. Carrier gas: air. Letters A–G refer to the segments described in Table 1.

Julia-based software package written by Dr. Cory Simon. NVT simulations of water used the TIP4P-Ew model for water.[50]

Initial adsorption sites and geometries for DMF periodic DFT calculations were obtained from simulated annealing calculations of one DMF molecule within the canonical (NVT) ensemble, using the force fields described above. The initial temperature for the simulated annealing calculations was 313 K, and this temperature was decreased by 2 to 4 K every 10^5 Monte Carlo steps. The simulation continued until the temperature reached 1.0 K.

Stiffness Tensor Calculation. The elements of the stiffness matrix were calculated on the basis of the crystal structure optimized with DFT using the setting mentioned above in the Periodic Density Functional Theory section, as the curvature of the potential energy surface with respect to lattice deformations. Finite difference approach to compute the energy penalty for different lattice deformations[51,52] was adopted. In-house code was used for generating the deformed structures and postprocessing the energy–strain outputs. For each element, five points were used to fit the second-order polynomial of energy–strain curves. The maximum strain for the calculation was set to 1%. ELATE, an online elastic tensor analysis package, was used for all the postprocessing on the stiffness matrix for extracting moduli of elasticity as well as for the visualization.[53]

RESULTS AND DISCUSSION

Crystal Structure Description. Self-assembly of Ca(II) ions with the H_4TBAPy ligand in an acidified mixture of DMF and water gave rise to the crystallization of $[Ca_2(TBAPy)(\mu_2\text{-}OH_2)_2]\cdot 2DMF$, hereafter **SION-8**, in the orthorhombic space group *Pbam*, as deduced from SCXRD analysis (see Table S1 for detailed crystallographic data). The asymmetric unit comprises a quarter of fully deprotonated $TBAPy^{4-}$ ligand, a half of a Ca(II) atom (Ca1 sitting on a special position with 0.50-occupancy), and a half of a H_2O molecule (Figure S1). The structure of **SION-8** is based on infinite 1-dimensional Ca–O chains extending along the *a*-axis (Figure 1a); O atoms in the chain originate from μ_2-bridging water molecules and from carboxylate functionalities of the ligand. The chains are connected to each other via $TBAPy^{4-}$, which coordinates to Ca(II) in $\eta^1{:}\eta^2$ bridging mode (Figure 1a); while O1 bonds to only one Ca1 atom, O2 is coordinated to two subsequent Ca1 atoms within the Ca–O chain. The overall coordination number of Ca(II) is 8, and the geometry of its coordination environment can be described as biaugmented trigonal prism (Figure S2). Topologically, Ca atoms can be considered as 6-coordinated nodes (two Ca1–O2 links can be severed in order to make the ligands conceptually $\eta^1{:}\eta^1$ bridging), bridging H_2O molecules as 2-coordinated nodes simplified to 2-coordinating links, and $TBAPy^{4-}$ ligands as 8-coordinated nodes. Following this description, the underlying net of **SION-8** is found to be of the ***sea*** type (Figure S3).

When two $TBAPy^{4-}$ ligands are attached to the same Ca1 atom (marked in orange in Figure 1c) with both O1 and O2 atoms, their planar pyrene cores are parallel to each other. At the same time, when sets of such ligands are coordinated to two subsequent Ca atoms of the Ca–O chain (accordingly marked in blue and orange in Figure 1c), they form an angle of 80.06°. This leads to the close-packed array of atoms in the (001) plane (Figure 1b) with the distance of 4.344 Å between two π-stacked $TBAPy^{4-}$ ligands.

However, in a perpendicular direction, the crystal packing is much looser. Infinite structural voids, depicted in Figure 1d, run through the entire crystal in parallel with the Ca–O chains. Responsible for the formation of these voids is the rectangular shape of the $TBAPy^{4-}$ ligand, with the pyrene core in the center and carboxylate groups situated far from it (Scheme 1). From the structural analysis, we learn that the chemical character of two symmetrically inequivalent channels running across the structure of **SION-8** is highly anisotropic. The voids located at the positions with x, 1/4, 0 coordinates are predominantly exposed to the lateral sides of $TBAPy^{4-}$ ligands, namely, the pyrene cores and benzoate rings, which clearly endow them with *hydrophobic* character. The cross section of these voids is 5.4 Å × 6.2 Å, excluding van der Waals radii, and the contribution from one such void to the unit-cell volume equals 105.5 $Å^3$ (4.6%). On the other hand, the channels situated at x, 0, 1/2 (5.9 Å × 10.0 Å large in cross section with the volume of 180 $Å^3$ corresponding to 7.8% of the unit cell), in addition to the pyrene cores and benzoate rings, are also surrounded by O atoms of the Ca–O chains and coordinated H_2O molecules, which allows us to refer to them as to *hydrophilic* pores. This observation is of high importance since only a few examples of MOFs with chemically distinctive pore types have been reported in the literature,[22,25,54–56] and making practical use of them, e.g., by taking up mutually incompatible molecules,[57] selective recognition of alcohol molecules,[58] or alternating the gas sorption properties,[59] has

DOI: 10.1021/acsami.8b13362
ACS Appl. Mater. Interfaces 2018, 10, 36144–36156

Table 1. Gradual Decrease of Mass of a Sample of SION-8 Recorded in the TGA Experiment Compared to the Values Based on the Formula Derived from SCXRD

segment	upper limit	loss of mass observed from TGA	loss of mass calculated from SCXRD	description
A	520 K	7.2%	7.8%	DMF in the hydrophobic pores
B	590 K	7.9%	7.8%	DMF in the hydrophilic pores
C	670 K	4.3%	3.8%	bridging H_2O molecules
D, E, F	915 K			framework decomposition
G		87.0%	79.4%	mineralized sample

been achieved only in a handful of them. More widely encountered are MOFs with chemically distinct types of nanocages.[60,61] The hydrophilicity/hydrophobicity of both pores of **SION-8** was confirmed by exploring the interaction of water with the two different pores via molecular simulation (Figure S4). A greater number of water molecules were found to preferentially occupy the hydrophilic pore (with the contribution of 81.28% to the atom residence) compared to the hydrophobic pore, thus demonstrating the hydrophilic nature of the former (Figure S4c). In addition, the hydrophilic pore showed a greater affinity (Q_{st} = −24(1) kJ/mol) to water at zero loading compared to the hydrophobic pore (Q_{st} = −14.90(2) kJ/mol). We note that in one unit cell of **SION-8** there are two hydrophilic and two hydrophobic pores (Figure 1d) accounting together for 571 Å^3 (24.8%) of its volume.

Bulk Characterization. The phase purity of bulk **SION-8** was confirmed through Le Bail fit of the PXRD pattern recorded with synchrotron radiation (Figure 2a). The PXRD pattern is retained upon the immersion of **SION-8** in water (Figure S5), proving its hydrolytic stability. The IR spectrum of **SION-8**, and in particular stretching vibrations of carbonyl group at 1590 cm^{-1} and an intense absorption band of extended aromatic ring at 1411 cm^{-1} (Figure S6), corroborate the incorporation of $TBAPy^{4-}$ ligand into the framework. Moreover, the broad band corresponding to the stretching vibrations of the carboxylic acid hydrogen at 3000 cm^{-1}, present in the spectrum of H_4TBAPy, is absent upon formation of **SION-8**, confirming that the $TBAPy^{4-}$ ligand is coordinated to Ca(II). The spectrum of **SION-8** also contains a weak signal at 1649 cm^{-1} originating from guest DMF molecules. TGA revealed an insight into the thermal stability of **SION-8** (Figure 2b). The TGA profile of **SION-8** does not show an abrupt drop of mass, but instead, the mass loss is realized in several steps. We can associate the two initial segments of the TGA profile to the release of guest DMF molecules residing within the pores; since the mass loss is not smooth in this region, we raise the hypothesis (see below for the experimental and computational evidence) that this release is stepwise: the DMF molecules trapped in the hydrophobic pores are removed first (below 520 K), while those remaining in the hydrophilic pores are removed at higher temperatures, up to 590 K. The decomposition of **SION-8** occurs only once the coordinated H_2O molecules are removed between 590 and 670 K, suggesting their vital role in maintaining the framework integrity. The experimental mass loss values match those based on the formula derived from SCXRD, $[Ca_2(TBAPy)(\mu_2\text{-}OH_2)_2]\cdot 2DMF$ (Table 1). The stepwise release of DMF molecules from the pores of **SION-8**, as strongly suggested by the TGA, prompted us to study the gradual activation of this material in an *in situ* SCXRD experiment.

Stepwise Activation. In order to further elucidate the gradual activation of **SION-8**, we designed an *in situ* SCXRD experiment (see the details in the Experimental Section) at BM01 (SNBL from ESRF). At high vacuum and at different temperatures, the **SION-8** structure was easily identified from all measurements, and the unit-cell volume and edge length changes are shown in Figures 3a and S7. The pore volume and content (expressed in the units of e$^-$) were quantified and plotted in Figure 3b,c. Upon temperature increase, the volume as well as the residual e$^-$ content of the hydrophilic pore are changed to a limited extent, despite the overall unit-cell volume increase from 2264 Å^3 at 300 K to 2368 Å^3 at 400 K as a consequence of thermal expansion. At the same time, the hydrophobic pore, while increasing only slightly its volume of about 120 Å^3, loses its excess electron density to a point that at 400 K it counts only 9 e$^-$. Comparing these results to the electron count of DMF, it is observed in this temperature range that the hydrophilic pore contains approximately 1 molecule of DMF, irrespective of temperature, while the hydrophobic pore loses its 1 molecule of DMF upon heating, and at 400 K, it is virtually empty. Therefore, at 400 K and under vacuum, the selective *partial activation* of **SION-8**, limited solely to its hydrophobic pore, can be achieved (Figure S8). We note that, on further heating, the single crystal of **SION-8** increased its mosaicity to a point that no sharp Bragg reflections could be recorded. The partially activated phase is referred to as **SION-8P**, while the phase where the pores of the framework are completely empty is named **SION-8F** (fully activated).

In order to investigate the molecular-level interactions responsible for the partial activation of **SION-8**, periodic DFT calculations were performed. The calculations show that, when DMF is present in a hydrophilic pore, the coordinated water molecule rotates, as compared to the empty structure, and facilitates the formation of a hydrogen bond between the water hydrogen atom and the DMF oxygen atom (Figure S9). Accordingly, DMF has a significantly greater binding energy in the hydrophilic pore than in the hydrophobic pore: 105 and 66 kJ/mol, respectively. The formation of this hydrogen bonding interaction helps explain why higher temperature is required to remove DMF from the hydrophilic pores. These findings are consistent with the partial activation of **SION-8** observed in the *in situ* SCXRD experiment and the infeasibility of the full activation while maintaining the crystal's singularity.

Framework Flexibility. Close examination of the crystal structure packing, described in the section Crystal Structure Description, prompted us to study the mechanical anisotropy of **SION-8**. The framework is composed of inorganic 1-dimensional Ca−O chains along the *a*-axis and of organic moieties in two other directions, resulting in a structure similar to the wine-rack-like frameworks, known for their interesting elastic properties.[62] Therefore, it is anticipated that **SION-8** can be particularly inflexible along the *a*-axis and much more flexible in the two perpendicular dimensions. In order to obtain further insight into the anisotropic flexibility of **SION-8**, three different computational approaches were pursued, all

DOI: 10.1021/acsami.8b13362
ACS Appl. Mater. Interfaces 2018, 10, 36144−36156

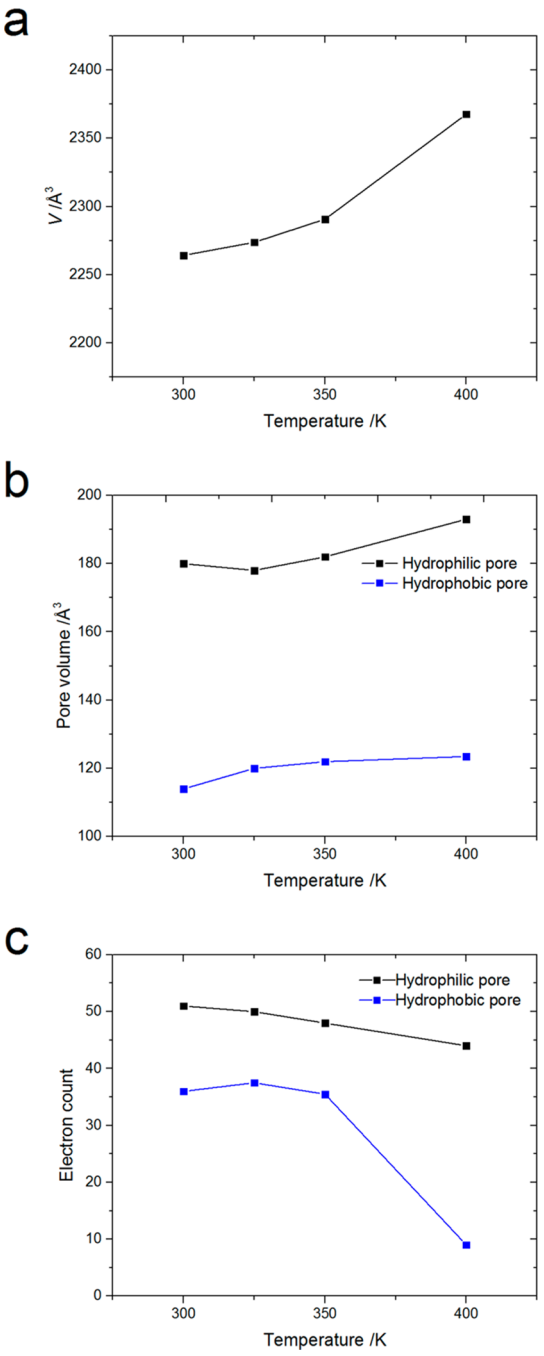

Figure 3. Stepwise activation of **SION-8** under vacuum investigated with SCXRD. (a) Volume, *V*, of the orthorhombic unit cell of **SION-8** plotted against temperature. (b) Volume of hydrophilic (black plots) and hydrophobic (blue plots) pores as calculated with SQUEEZE. (c) Excess electron density per pore found in both types of pores. Note that there are two hydrophobic and two hydrophilic pores in each unit cell.

using **SION-8F** as a model. First, we examined the mechanical properties of the structure using DFT and computed the complete stiffness tensor (Scheme S1), which according to the theory of elasticity, describes the mechanical properties of a crystal in the elastic regime, i.e., the region where a crystal recovers its original shape when the stress is removed.[63] The Young's modulus, i.e., the resistance of a material to uniaxial stress, was then extracted from it and presented in a geometrical form (Figures 4a and S10).

The 3-dimensional representation of Young's modulus showcases the mechanical anisotropy of **SION-8**, which can be rationalized by linking the stress-induced changes of the unit-cell parameters to the strain of geometric features at the microscopic level. The material is very stiff along the *a*-axis, with Young's modulus of 12.4 GPa, the parameter *a* equaling the pitch of the zigzag array of Ca atoms found in the 1-dimensional Ca−O chains (Figure 4b). Upon the influence of the mechanical stress, this axis experiences hardly any change as within the Ca−O chains the Ca coordination polyhedra can undergo rotations or other deformations relative to one another, but they are particularly inflexible. From the 3-dimensional representation of the Young's modulus, a considerable stiffness of the material along approximately the [011] direction, of 7.7 GPa, corresponding to the rigid arms of the $TBAPy^{4-}$ ligand (Scheme 1), is also clearly appreciable. A higher level of flexibility is exhibited by the parameter *c*, along which Young's modulus drops to 4.9 GPa, and which represents the hydrophobic pore length (Figure 4c); however, as with the parameter *a*, it is dependent strictly on the geometry of Ca−O polyhedra. From the side of the ligand, this pore length is constrained by all-sp^2 hybridization of C atoms within $TBAPy^{4-}$ which allows only some specific values of bond angles. Therefore, the *c* dimension can be altered only to a certain extent. The polyhedra rotation can however have tremendous impact on the angle between the Ca−O chains and the $TBAPy^{4-}$ ligand struts in the [001] plane (Figure 4b), which directly influences the *b* axis length. Moreover, even a slight deformation of Ca-based polyhedra can result in a considerable reorientation of $TBAPy^{4-}$ in this plane, and since the Ca−O vs $TBAPy^{4-}$ angle can assume a wide range of values, **SION-8** exhibits the highest flexibility along the *b* axis (Figure 4a), which is reflected by the low value of Young's modulus of 0.8 GPa along this axis. The anisotropy of Young's modulus, i.e., the ratio between its maximum and minimum values, of 15.5, places **SION-8** among materials of intermediate anisotropy, along with those classified as reinforced wine-rack, e.g., MIL-140A. Typically, flexible MOFs, e.g., MIL-53, have a very large anisotropy factor (∼100), while rigid MOFs, e.g., ZIF-8 and UiO-66, have an anisotropy factor of around 1.[64]

In addition, we performed DFT calculations for **SION-8** with deliberately chosen values of the unit-cell dimension *b*, changing it up to ±10% and allowing the lattice parameters *a* and *c*, and the atomic coordinates of the entire structure, to relax to the minimum energy. The energy difference between these structures was subsequently assessed (Figure S11). Compressing or stretching the *b* dimension by up to 2 Å from the *b* corresponding to the minimum-energy structure incurs an energy penalty of less than 7 kJ/mol, which is less than the adsorption enthalpy of the gases studied (*vide infra*). Hence, it is suspected that, upon gas adsorption, adsorption-accommodating unit-cell deformations could be observed.

Finally, we computed coefficients of thermal expansion along the three crystallographic axes via a slow annealing NPT Molecular Dynamics simulation. From them, it is deduced that **SION-8F** exhibits a negative thermal expansion along the axis *c*, a very weak positive thermal expansion along *a*, and a particularly strong positive thermal expansion along *b*, which provides still further evidence of the framework flexibility in the *b* direction (Figure S12).

Response of the Structure to N_2, CO_2, and CH_4 Adsorption and Temperature Changes. Structural flexibility may lead to drastic alterations of the adsorption capacity

DOI: 10.1021/acsami.8b13362
ACS Appl. Mater. Interfaces 2018, 10, 36144−36156

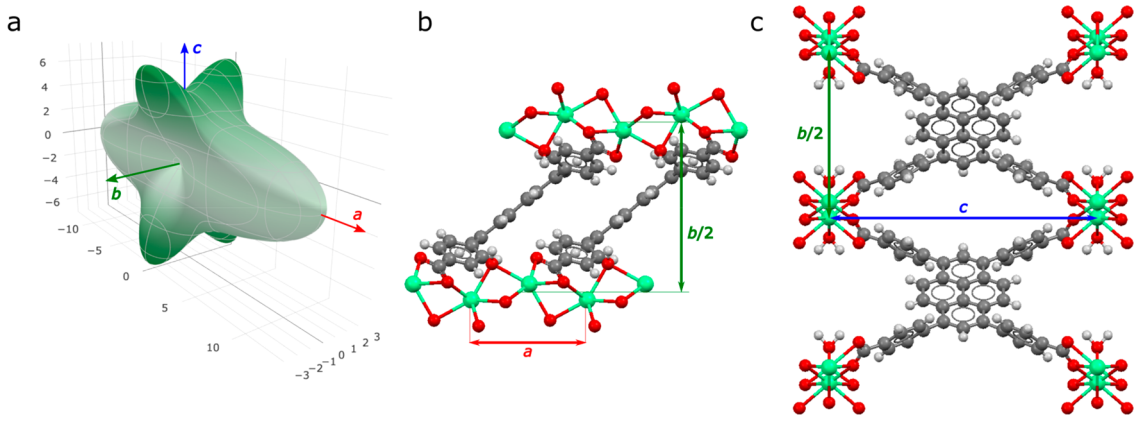

Figure 4. (a) 3-dimensional representation of Young's modulus (in GPa) of **SION-8**. Side view of this representation is presented in Figure S10. The anisotropy of the crystal's compliance is clearly appreciable. (b) View in the [001] plane and (c) view in the [100] plane of the crystal structure of **SION-8** highlighting the unit-cell parameters of different flexibilities.

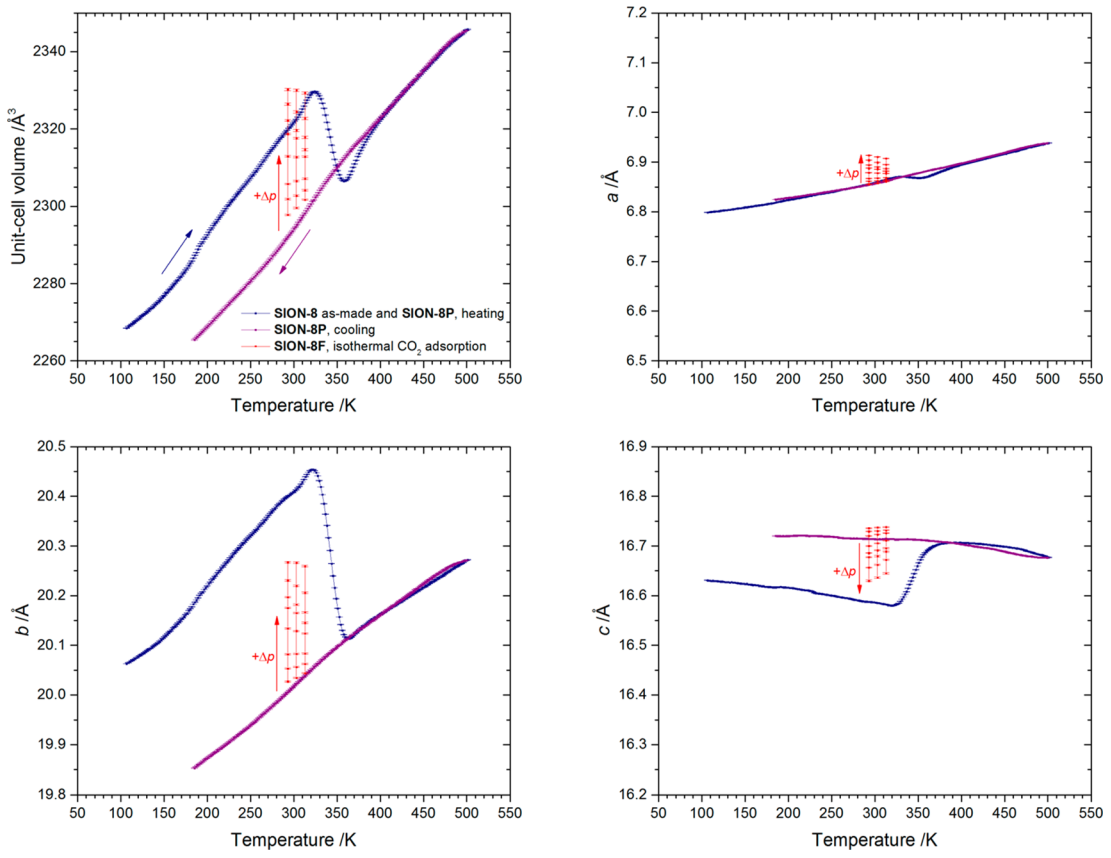

Figure 5. Unit-cell volume and parameters *a*, *b*, and *c* derived from Le Bail fits of the VT PXRD patterns. Fully solvated **SION-8** undergoes a 1.0% unit-cell compression at 325−360 K upon heating (blue plots), associated with the transformation to **SION-8P**. The cooling run (purple plots) does not show an analogous feature. Isothermal data for **SION-8F** at different pressures of CO_2 (Figure S17) are overlaid in red.

of a porous material. In particular, flexibility in a MOF can either improve or reduce its performance, mainly because of the impact on the pore size and shape.[65] For this reason, the flexibility of **SION-8** was studied as a function of the external gas pressure with SCXRD and PXRD chosen as experimental techniques to monitor the mechanical changes.

SCXRD was used first for two reasons: it provides information on the unit-cell parameter changes caused by the gas adsorption, and simultaneously, it can give insights on how the external gas pressure influences the crystal structure. A single crystal of **SION-8P** was subjected to high pressures of N_2, CO_2, and CH_4 (see details in the Experimental Section), and the corresponding crystal structures were solved and refined at each pressure point of these isotherms.

It was found that the gas molecules are adsorbed within the hydrophobic pores of **SION-8P**, but instead of assuming well-defined positions, they are heavily disordered; therefore, we turned to the integration of electron density as an adsorption probing tool. The amount of adsorbate was found to depend on the nature of the gas. At the studied conditions, a practically negligible amount of N_2 (Figure S13) is adsorbed in the pores, as we noticed no significant changes in the electron count

DOI: 10.1021/acsami.8b13362
ACS Appl. Mater. Interfaces 2018, 10, 36144−36156

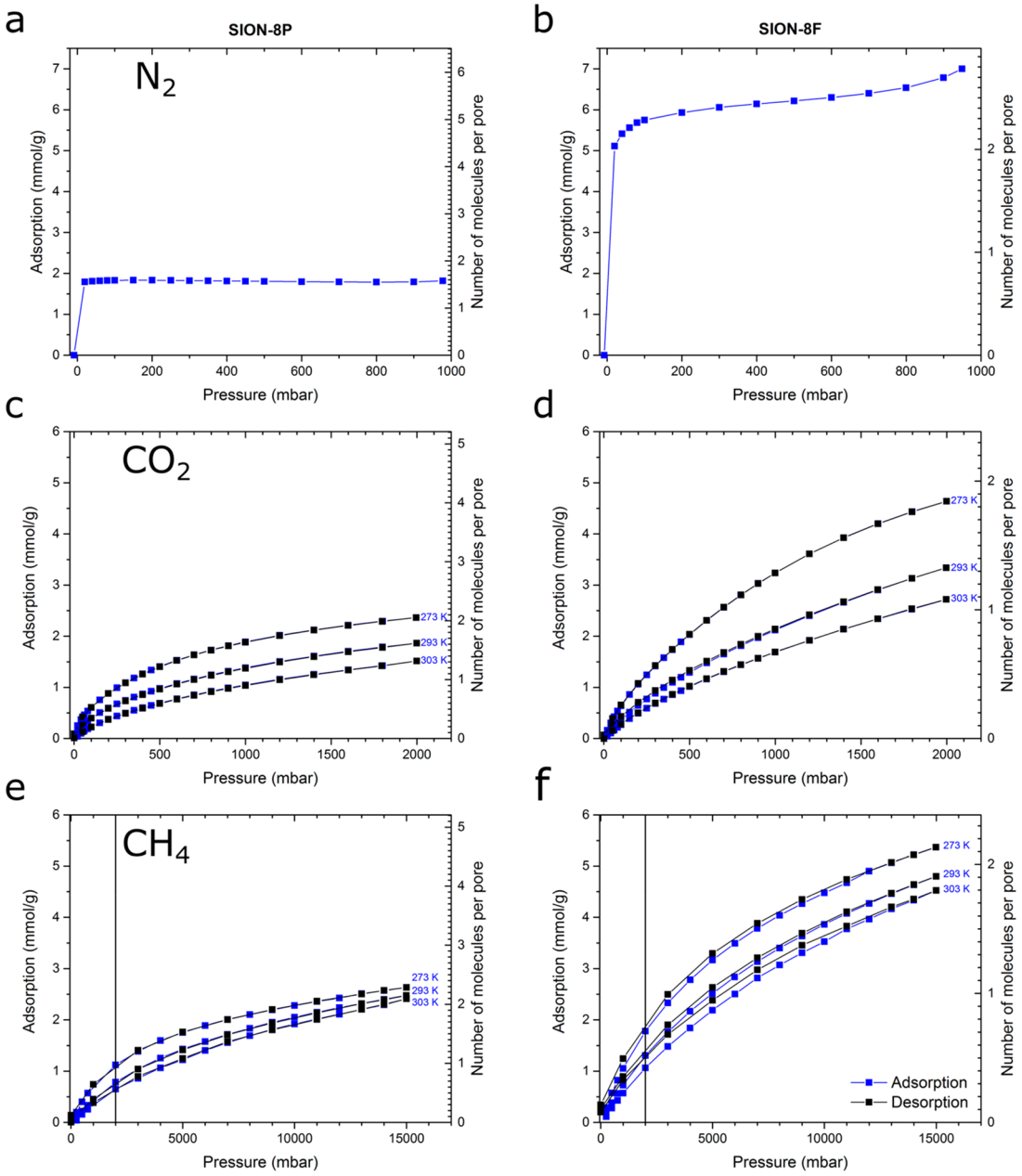

Figure 6. Experimental N_2-adsorption isotherm of **SION-8P** (a) and of **SION-8F** (b) at 77 K; experimental CO_2-adsorption isotherms of **SION-8P** (c) and of **SION-8F** (d) at 273, 293, and 303 K; experimental CH_4-adsorption isotherms of **SION-8P** (e) and of **SION-8F** (f) at 273, 293, and 303 K. Vertical line in the panels e and f represents the pressure of 2000 mbar.

within the structural voids. Similarly, upon increased external CH_4 pressure, an increase of 5.5 e^- of the integrated electron density within the hydrophobic pore is interpreted as the adsorption of less than 1 molecule of CH_4 in 1 hydrophobic pore (Figure S14). However, upon CO_2 adsorption, the excess electron count within the hydrophobic pores gradually increased by ~30 e^- (Figure S15). Therefore, each hydrophobic pore in **SION-8P**, once evacuated as a result of the activation process, can be filled with ~1.5 molecules of CO_2. The CO_2 adsorption within **SION-8P** monitored directly by SCXRD can be modeled with the Langmuir adsorption isotherm equation (Figure S16) resembling the isotherms recorded with the gravimetric method (*vide infra*).

Comparing the changes of the pore content induced by the external gas pressure with the concomitant evolution of the unit-cell dimensions (Figures S13–S15), it becomes clear that the most noticeable structural changes in **SION-8P** are exerted by CO_2. The influence of CO_2 on **SION-8P** is 2-fold: the uniform external pressure compresses the crystallites, and simultaneously, due to their porous nature, their pores are gradually filled with an increasing number of CO_2 molecules; as can be seen from the pressure dependence of the unit-cell volume (Figure S15), the second phenomenon prevails. When the external pressure of CO_2 is increased, the parameter *a* elongates to a small extent and the parameter *b*, to a considerable extent, while the unit-cell dimension *c* shrinks; the magnitude of these deformations is analogous to that predicted from the Young's modulus calculation. The process is linked to an overall appreciable increase in volume of both the hydrophobic and the hydrophilic pores. These data are

DOI: 10.1021/acsami.8b13362
ACS Appl. Mater. Interfaces 2018, 10, 36144–36156

Table 2. Comparison between the Two Sets of Activation Conditions Leading to Two Activation Stages, SION-8P and SION-8F

	SION-8P	SION-8F
activation conditions	403 K, vacuum, 8 h	solvent exchanged to acetone, 463 K, vacuum, 8 h
observed loss of mass	8.7%	15.5%
loss of mass calculated from TGA	7.2%	15.1%
loss of mass calculated from the molecular formula	7.8% $[Ca_2(TBAPy)(H_2O)_2]\cdot DMF$	15.6% $[Ca_2(TBAPy)(H_2O)_2]$
pore volume derived from the isotherm	0.0826 cm^3/g	0.2280 cm^3/g
pore volume derived from the crystal structure	0.0724 cm^3/g	0.2164 cm^3/g
BET surface area	174 m^2/g	509 m^2/g

representative, since the same trends are observed when crystalline powder of **SION-8F** is subjected to CO_2, and the unit-cell parameters are derived from *in situ* recorded PXRD patterns (Figure S17).

An analogous response is exhibited by the as-made **SION-8** material when subjected to still another external stimulus, namely, variable temperature (Figure 5). Initially, the pores of the material are filled with noncoordinated DMF molecules, and upon heating, the unit cell experiences the uniform changes of its volume and edge lengths, in line with the computational prediction of thermal expansion. However, in the 325−360 K temperature range, the unit-cell volume drops by 1.0% on heating, which we associate with the partial desolvation and generation of **SION-8P**.[66] This structural change is anisotropic as it is primarily realized along the *b* axis. After this transition, the desolvated structure changes monotonically in the same manner as before the transition, which turns out to be irreversible (once the solvent molecules are released from the pores, the mechanical response of the framework is not impeded by any factor). We therefore reason that, in order to accommodate guest species within its pores, **SION-8** shrinks along *c*, elongates to a significant extent along *b*, and stays virtually invariant along *a*. Ultimately, the uptake of guest molecules exhibited by **SION-8** is greatly enhanced by its flexibility. Virtually, the same structural mechanisms play a role upon an increased external pressure of CO_2 (Figure 5); in order to accommodate CO_2 gas molecules, **SION-8** anisotropically enhances its volume. In this respect, the behavior of **SION-8** resembles that of Co(bdp)[13] and MIL-53(Cr),[67] although in both of these cases the accommodation of additional gas molecules is realized upon phase transitions toward the forms of higher capacity, rather than through continuous structural changes within the same phase.

Single-Component N_2, CO_2, and CH_4 Adsorption. Adsorption of different gases, N_2, CO_2, and CH_4, in the hydrophobic pores of **SION-8P**, observed in the *in situ* SCXRD experiment, prompted us to study further the sorption properties of the bulk material. First, we activated the powdered sample of **SION-8** using the previously discussed conditions for 8 h and measured the N_2-sorption isotherm at 77 K (Figure 6a). The mass loss observed prior to the isotherm collection is in agreement with the loss observed from TGA and crystallographic analysis (Table 2). Application of the Brunauer−Emmett−Teller (BET) model resulted in the surface area estimate of 174 m^2/g, while the calculated pore volume of 0.0826 cm^3/g was comparable to the one derived from the crystal structure. As expected, **SION-8** does not lose crystallinity upon activation and subsequent N_2 adsorption (Figure S18).

SION-8F, i.e., the *fully activated* phase in which both types of pores are emptied and available for gas adsorption, was achieved in the bulk by exploring another set of activation conditions, sample immersed in acetone for 3 days and subsequently outgassed at 463 K for 8 h with a membrane vacuum pump, as evidenced by the comparison between the measured and calculated values of loss of mass and pore volume (Table 2). Moreover, the values of N_2 uptake (Figure 6b) were found to be in line with the computational prediction (Figure S19), and a 3-fold increase in BET surface area (Table 2) was recorded.

Therefore, by changing the activation conditions, we gained access to two bulk materials of different sorption properties. Most importantly, we observed that the isotherms collected on **SION-8P** were reproducible: due to the strong interactions between DMF and the hydrophilic pore (*vide supra*), its evacuation was efficiently delayed while the hydrophobic pore was already activated. **SION-8P** and **SION-8F** were additionally tested for CO_2 and CH_4 adsorption at 273, 293, and 303 K (Figure 6c−f); in both cases, the sorption performance of **SION-8F** was nearly two times that of **SION-8P**. On the basis of the pore volume determined from SCXRD at 300 K (Figure 3) and the molecular volume of CH_4,[68] one hydrophobic pore of **SION-8** can theoretically accommodate ∼1.7 molecules of CH_4, while one hydrophilic pore has a maximum capacity of ∼2.8 molecules of CH_4 (therefore, the average equals ∼2.3 molecules). Simultaneously, from single-component adsorption isotherms at 303 K and 15 000 mbar (Figure 6e,f), we observed a preference for the pores to be occupied by 2.0 molecules of CH_4 in the hydrophobic pore (**SION-8P**) and by an average of 1.8 molecules of CH_4 per pore in **SION-8F**. This provides qualitative confirmation that the actual size of the pores is the limiting factor of CH_4 adsorption capacity. A similar conclusion can be drawn for the adsorption of CO_2.[69] The flexibility of this MOF and the complex effect of guest adsorption on the structure make this a challenging MOF to model computationally; thus, CO_2 and CH_4 isotherms computed from molecular simulations in both **SION-8F** and **SION-8P** deviate from experimental isotherms (Figure S20). However, the satisfactory agreement at low pressures led us to use this model for qualitative insight on adsorption.

The isosteric heats of adsorption Q_{st} calculated from the experimental isotherms reflect the energy of interaction between the studied gas species and the pore surface in **SION-8P** and **SION-8F** (Table 3). In **SION-8P**, we associate the Q_{st} with the energy of interaction between the gas and the hydrophobic pore. In **SION-8F**, however, interactions between gas and both types of pores, the hydrophobic and the hydrophilic one, contribute to the overall Q_{st} (the energy of the gas−hydrophilic pore interaction is not experimentally available). CO_2 interacts more strongly with the pores than does CH_4 in both materials. This opens up a possibility to use **SION-8** in CO_2/CH_4 separations. Furthermore, in **SION-8P**,

DOI: 10.1021/acsami.8b13362
ACS Appl. Mater. Interfaces 2018, 10, 36144−36156

Table 3. Isosteric Heats of Adsorption Q_{st} at Zero Loading Calculated from CH_4 and CO_2 Adsorption Isotherms Recorded at Different Temperatures for SION-8P and SION-8F[a]

	SION-8P (only hydrophobic pores accessible)	**SION-8F** (both pores accessible)
CH_4	21.4	16.0
CO_2	28.4	23.4

[a]Values in kJ/mol.

the interaction between CO_2 and the pores is 1.3 times stronger than the analogous interaction of CH_4; in **SION-8F**, this ratio increases to 1.5. Consequently, the CO_2/CH_4 separation is expected to be more efficient with **SION-8F**. In order to gain further insights into the interactions of CO_2 and CH_4 in each pore independently, we used molecular simulations to compute the heats of adsorption in each individual pore as well as in the fully activated structure as a function of loading (Figure S21). Both CO_2 and CH_4 are more strongly bound in the hydrophobic pore, and CO_2 is overall more strongly bound than CH_4. Interestingly, for both CO_2 and CH_4, the Q_{st} of **SION-8F** was found not to be a simple average of energies of interaction between the hydrophilic pore and the hydrophobic pore (Figure S21).

The trends in the energy of interaction between adsorbates and pore surfaces in **SION-8F** compared to **SION-8P** can further be understood by examining the simulated probability density of CO_2 and CH_4 locations in both materials (Figure 7). CO_2 is only slightly more preferentially adsorbed in the hydrophobic pore compared to the hydrophilic one, thus reflecting the small difference in respective heats of adsorption. CH_4, however, shows greater preference for the hydrophobic pore than CO_2 does. This is still additional evidence suggesting that, when the hydrophilic pore is available as in **SION-8F**, the ratio of CO_2 to CH_4 adsorbed shall increase, thereby increasing the CO_2/CH_4 selectivity.

CO_2/CH_4 Separation. Prompted by the significantly different isosteric heats of adsorption derived from single-component adsorption isotherms and GCMC simulations, the CO_2/CH_4 separation performance of **SION-8P** and **SION-8F** was further investigated with breakthrough experiments, which provide additional information on the adsorption kinetics as compared with the equilibrium isotherms. A range of different CO_2/CH_4 gas mixtures were tested, with the focus on 90% CH_4 and 10% CO_2 (model composition of acid natural gas) and on 50% CH_4 and 50% CO_2 (model composition of biogas). As can be seen from the recorded breakthrough curves (Figure S22), at each condition, CH_4 was released from the chromatographic column first, followed by CO_2 after a certain retention time spanning from several seconds to minutes. Adsorption capacities of **SION-8P** and **SION-8F** were calculated by integrating breakthrough curves (Table S2) and were further used for the calculation of CO_2/CH_4 dynamic breakthrough selectivities, α, summarized in Table 4. In all cases, α is higher than 1, implying that, indeed in contact with the CO_2/CH_4 mixture, **SION-8P** and **SION-8F** selectively adsorb CO_2 over CH_4. The CO_2/CH_4 separation is more efficient at lower concentrations of CO_2, which require lower adsorbed amounts of CO_2 for an equally efficient separation, and at lower temperature, which favors the increase in CO_2 adsorption capacity more as compared to that of CH_4 (Table S2). The better performance of **SION-8F** compared to **SION-8P**, increased by 40% in the case of a mixture of 90% CH_4 and 10% CO_2 at 323 K and nearly 3-fold for the same gas mixture at 273 K (Table 4), is a consequence of different CO_2/CH_4 Q_{st} ratios exhibited by these materials. **SION-8F** showed the best separation performance toward the mixture composed of 90% CH_4 and 10% CO_2, and it decreased toward more moderate values with the increased concentrations of CO_2. Similar

Table 4. CO_2/CH_4 Dynamic Breakthrough Selectivities, α, for SION-8F and SION-8P Calculated from the Integration of the Respective Breakthrough Curves Recorded at 273, 303, and 323 K and at a Range of CO_2/CH_4 Relative Molar Ratios

	SION-8F				
	10% CH_4, 90% CO_2	25% CH_4, 75% CO_2	50% CH_4, 50% CO_2	75% CH_4, 25% CO_2	90% CH_4, 10% CO_2
273 K	2.16	2.16	3.09	5.42	5.45
303 K	1.69	1.73	2.34	3.16	3.71
323 K	1.49	1.55	1.62	1.94	1.98
	SION-8P				
	10% CH_4, 90% CO_2	25% CH_4, 75% CO_2	50% CH_4, 50% CO_2	75% CH_4, 25% CO_2	90% CH_4, 10% CO_2
273 K	1.10				2.11
303 K	1.01			1.41	1.47
323 K					1.38

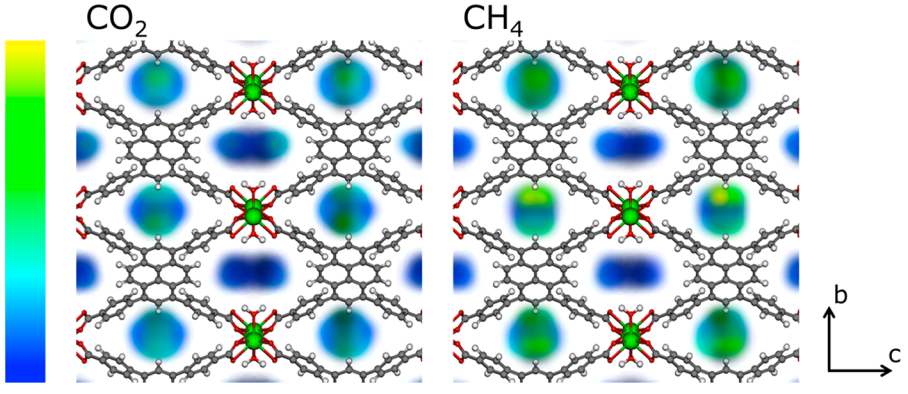

Figure 7. Probability density plots of adsorbate positions in **SION-8F**, generated from Monte Carlo NVT simulations with 2 molecules per unit cell, at 293 K. The color bar on the left denotes low (blue) to high (yellow) relative probability. CO_2 has 61.9% and 38.1% occupation in the hydrophobic and hydrophilic pores, respectively, while CH_4 has 66.1% and 33.9% occupation. See Figure S23 for side view of channels.

DOI: 10.1021/acsami.8b13362
ACS Appl. Mater. Interfaces 2018, 10, 36144−36156

dependence of the selectivity on the CO_2/CH_4 mixture composition was previously found in other materials selective to CO_2, e.g., in MIL-101(Al)-NH_2,[70] MIL-53(Al)-NH_2,[71] and CCP-1.[72] We note that the values of selectivities derived from breakthrough curves arise from practical separation processes, in contrast to the selectivities calculated from single-component isotherms, which reflect the idealized situation and should only be used as upper-level approximations. Therefore, the comparison of the separation performance of **SION-8** can be made where the selectivity of materials was calculated through the breakthrough experiments (Table S3). With its CO_2/CH_4 dynamic breakthrough selectivity of 2.34 toward the 50% CH_4 and 50% CO_2 gas mixture at 303 K, **SION-8F** performs similarly well compared to other MOFs based on ligands with aromatic groups exposed to the pore surfaces (e.g., MOF-508b, α = 3;[73] MIL-101(Cr), α = 3.6);[35] however, MOFs containing unobstructed amino functionalization (e.g., MIL-101(Al)-NH_2, α = 6.3;[70] MIL-53(Al)-NH_2, α = 45)[71] or negatively charged SiF_6^{2-} groups within the pores (e.g., SIFSIX-2-Cu-i, α = 51)[10] perform better. Nevertheless, **SION-8** has a tunable separation performance, which to the best of our knowledge has not been reported earlier.

CONCLUSIONS

SION-8, a novel biporous MOF endowed with two chemically contrasting structural pores, the hydrophobic and the hydrophilic, was successfully synthesized and fully characterized with diffraction, spectroscopic, and thermogravimetric methods. By judiciously altering the activation conditions, two functional materials were obtained: the partially activated **SION-8P** and the fully activated **SION-8F**. Due to their distinct pore environments, **SION-8P** and **SION-8F** showed different adsorption properties toward N_2, CO_2, and CH_4, and the size of the available pores was found to be the limiting factor for gas adsorption. Intrinsic structural flexibility, exhibited by **SION-8** primarily along the *b*-axis as anticipated through computations, was found to be responsible for the structural adjustments allowing for the accommodation of guest solvent and gas molecules. The tunable CO_2/CH_4 separation performance was tested with breakthrough experiments at 1 bar and expressed in terms of the CO_2/CH_4 dynamic breakthrough selectivity factors, α. At 273 K, **SION-8P** showed α of 2.11 toward the gas mixture composed of 90% CH_4 and 10% CO_2, while the respective value for **SION-8F** reached 5.45. A significant contrast between the values of Q_{st} and probability density of CO_2 and CH_4 locations in the two chemically different pores constitutes the rationale behind the different dynamic breakthrough selectivity factors in both materials. The discovery of **SION-8** and the link between the macroscopic properties and the underlying chemistry of this material bring us closer to the rational design of new materials that can be used for a plethora of applications such as natural gas purification and other energy-related separations.

ASSOCIATED CONTENT

Supporting Information

The Supporting Information is available free of charge on the ACS Publications website at DOI: 10.1021/acsami.8b13362.

Detailed crystallographic and topological data, results of DFT calculations and MD and GCMC simulations, additional SCXRD, PXRD, IR, and adsorption data, breakthrough curves and the interpretation thereof (PDF)

CIF file of **SION-8** (CIF)

AUTHOR INFORMATION

Corresponding Author

*E-mail: kyriakos.stylianou@epfl.ch.

ORCID

Iurii Dovgaliuk: 0000-0003-1997-4748
Peter G. Boyd: 0000-0001-6541-0594
Seyed Mohamad Moosavi: 0000-0002-0357-5729
Daniele Ongari: 0000-0001-6197-2901
Jorge A. R. Navarro: 0000-0002-8359-0397
Berend Smit: 0000-0003-4653-8562
Kyriakos C. Stylianou: 0000-0003-1670-0020

Author Contributions

A.G. performed all experiments described in the manuscript. A.G. and I.D. conducted the gas loading single crystal and powder X-ray diffraction experiments and analyzed the data. A.C. and J.A.R.N. performed and analyzed the breakthrough experiments. K.S.D., K.Y.O., P.G.B., S.M.M., D.O., and B.S. performed the simulations reported in the manuscript. K.C.S. led the project, and A.G., K.S.D., and K.C.S. wrote the manuscript with contributions from all coauthors.

Notes

The authors declare no competing financial interest.

ACKNOWLEDGMENTS

K.C.S. thanks the Swiss National Science Foundation (SNF) for funding under the Ambizione Energy Grant n.PZENP2_166888. P.G.B. is supported by the European Research Council (FP/2007−2013)/ERC Grant Agreement n.666983 − MaGic. The access to the BM01 and BM31 beamlines at the ESRF, Grenoble, France, is greatly acknowledged. A.G. and K.C.S. thank Dr. Dmitry Chernyshov for help and support. A.G. is grateful to Prof. Davide M. Proserpio for fruitful discussions. K.Y.O. thanks the John Stauffer Endowment for the Undergraduate Summer Research Program in the College of Chemistry. The Swiss National Supercomputing Centre (CSCS) under project no.s611 supported this work. Classical simulations and ab initio calculations (K.S.D.) are based upon work supported by the National Science Foundation Graduate Research Fellowship Program under Grant No. DGE 1106400, as well as by the Center for Gas Separations Relevant to Clean Energy Technologies, an Energy Frontier Research Center funded by the U.S. Department of Energy, Office of Science, Basic Energy Sciences under Award # DE-SC0001015. DFT calculations (K.S.D.) used resources of the National Energy Research Scientific Computing Center, a DOE Office of Science User Facility supported by the Office of Science of the U.S. Department of Energy under the Contract No. DE-AC02-05CH11231. J.A.R.N. thanks Spanish MINECO (CTQ2017-84692-R) and EU Feder funding.

REFERENCES

(1) Rochelle, G. T. Amine Scrubbing for CO_2 Capture. *Science* **2009**, *325*, 1652−1654.
(2) Ruthven, D. M. *Principles of Adsorption and Adsorption Processes*; Wiley: New York, 1984.
(3) Kidnay, A. J.; Parrish, W. R. *Fundamentals of Natural Gas Processing*; Taylor & Francis: Boca Raton, FL, 2006.

DOI: 10.1021/acsami.8b13362
ACS Appl. Mater. Interfaces 2018, 10, 36144−36156

(4) Gomez, L. F.; Zacharia, R.; Bénard, P.; Chahine, R. Multicomponent Adsorption of Biogas Compositions Containing CO_2, CH_4 and N_2 on Maxsorb and Cu-BTC Using Extended Langmuir and Doong−Yang Models. *Adsorption* **2015**, *21*, 433−443.
(5) Baker, R. W.; Lokhandwala, K. Natural Gas Processing with Membranes: An Overview. *Ind. Eng. Chem. Res.* **2008**, *47*, 2109−2121.
(6) D'Alessandro, D. M.; Smit, B.; Long, J. R. Carbon Dioxide Capture: Prospects for New Materials. *Angew. Chem., Int. Ed.* **2010**, *49*, 6058−6082.
(7) Böttcher, C. J. F.; Bordewijk, P. *Theory of Electric Polarization*; Elsevier: Amsterdam, 1978.
(8) Masala, A.; Vitillo, J. G.; Mondino, G.; Grande, C. A.; Blom, R.; Manzoli, M.; Marshall, M.; Bordiga, S. CO_2 Capture in Dry and Wet Conditions in UTSA-16 Metal−Organic Framework. *ACS Appl. Mater. Interfaces* **2017**, *9*, 455−463.
(9) Pato-Doldán, B.; Rosnes, M. H.; Dietzel, P. D. C. An In-Depth Structural Study of the Carbon Dioxide Adsorption Process in the Porous Metal−Organic Frameworks CPO-27-M. *ChemSusChem* **2017**, *10*, 1710−1719.
(10) Nugent, P.; Belmabkhout, Y.; Burd, S. D.; Cairns, A. J.; Luebke, R.; Forrest, K.; Pham, T.; Ma, S.; Space, B.; Wojtas, L.; Eddaoudi, M.; Zaworotko, M. J. Porous Materials with Optimal Adsorption Thermodynamics and Kinetics for CO_2 Separation. *Nature* **2013**, *495*, 80−84.
(11) Demessence, A.; D'Alessandro, D. M.; Foo, M. L.; Long, J. R. Strong CO_2 Binding in a Water-Stable, Triazolate-Bridged Metal−Organic Framework Functionalized with Ethylenediamine. *J. Am. Chem. Soc.* **2009**, *131*, 8784−8786.
(12) McDonald, T. M.; Mason, J. A.; Kong, X.; Bloch, E. D.; Gygi, D.; Dani, A.; Crocellà, V.; Giordanino, F.; Odoh, S. O.; Drisdell, W. S.; Vlaisavljevich, B.; Dzubak, A. L.; Poloni, R.; Schnell, S. K.; Planas, N.; Lee, K.; Pascal, T.; Wan, L. F.; Prendergast, D.; Neaton, J. B.; Smit, B.; Kortright, J. B.; Gagliardi, L.; Bordiga, S.; Reimer, J. A.; Long, J. R. Cooperative Insertion of CO_2 in Diamine-appended Metal-organic Frameworks. *Nature* **2015**, *519*, 303.
(13) Mason, J. A.; Oktawiec, J.; Taylor, M. K.; Hudson, M. R.; Rodriguez, J.; Bachman, J. E.; Gonzalez, M. I.; Cervellino, A.; Guagliardi, A.; Brown, C. M.; Llewellyn, P. L.; Masciocchi, N.; Long, J. R. Methane Storage in Flexible Metal−organic Frameworks with Intrinsic Thermal Management. *Nature* **2015**, *527*, 357.
(14) Sumida, K.; Rogow, D. L.; Mason, J. A.; McDonald, T. M.; Bloch, E. D.; Herm, Z. R.; Bae, T.-H.; Long, J. R. Carbon Dioxide Capture in Metal−Organic Frameworks. *Chem. Rev.* **2012**, *112*, 724−781.
(15) He, Y.; Zhou, W.; Qian, G.; Chen, B. Methane Storage in Metal−organic Frameworks. *Chem. Soc. Rev.* **2014**, *43*, 5657−5678.
(16) Kreno, L. E.; Leong, K.; Farha, O. K.; Allendorf, M.; Van Duyne, R. P.; Hupp, J. T. Metal−Organic Framework Materials as Chemical Sensors. *Chem. Rev.* **2012**, *112*, 1105−1125.
(17) Andrzejewski, M.; Katrusiak, A. Piezochromic Porous Metal−Organic Framework. *J. Phys. Chem. Lett.* **2017**, *8*, 279−284.
(18) Barea, E.; Montoro, C.; Navarro, J. A. R. Toxic Gas Removal − Metal−organic Frameworks for the Capture and Degradation of Toxic Gases and Vapours. *Chem. Soc. Rev.* **2014**, *43*, 5419−5430.
(19) Rodríguez-Albelo, L. M.; López-Maya, E.; Hamad, S.; Ruiz-Salvador, A. R.; Calero, S.; Navarro, J. A. R. Selective Sulfur Dioxide Adsorption on Crystal Defect Sites on an Isoreticular Metal Organic Framework Series. *Nat. Commun.* **2017**, *8*, 14457.
(20) Gładysiak, A.; Nguyen, T. N.; Navarro, J. A. R.; Rosseinsky, M. J.; Stylianou, K. C. A Recyclable Metal−Organic Framework as a Dual Detector and Adsorbent for Ammonia. *Chem. - Eur. J.* **2017**, *23*, 13602−13606.
(21) Liu, Y.; Howarth, A. J.; Vermeulen, N. A.; Moon, S.-Y.; Hupp, J. T.; Farha, O. K. Catalytic Degradation of Chemical Warfare Agents and Their Simulants by Metal-organic Frameworks. *Coord. Chem. Rev.* **2017**, *346*, 101−111.
(22) Chaudhari, A. K.; Mukherjee, S.; Nagarkar, S. S.; Joarder, B.; Ghosh, S. K. Bi-porous Metal−organic Framework with Hydrophilic and Hydrophobic Channels: Selective Gas Sorption and Reversible Iodine Uptake Studies. *CrystEngComm* **2013**, *15*, 9465−9471.
(23) Sapchenko, S. A.; Samsonenko, D. G.; Dybtsev, D. N.; Fedin, V. P. Hierarchical Guest Exchange and Step-by-Step Activation of a Biporous Coordination Framework. *Inorg. Chem.* **2013**, *52*, 9702−9704.
(24) Ohmori, O.; Kawano, M.; Fujita, M. A Two-in-One Crystal: Uptake of Two Different Guests into Two Distinct Channels of a Biporous Coordination Network. *Angew. Chem., Int. Ed.* **2005**, *44*, 1962−1964.
(25) Abrahams, B. F.; Moylan, M.; Orchard, S. D.; Robson, R. Zinc Saccharate: A Robust, 3D Coordination Network with Two Types of Isolated, Parallel Channels, One Hydrophilic and the Other Hydrophobic. *Angew. Chem.* **2003**, *115*, 1892−1895.
(26) Stylianou, K. C.; Heck, R.; Chong, S. Y.; Bacsa, J.; Jones, J. T. A.; Khimyak, Y. Z.; Bradshaw, D.; Rosseinsky, M. J. A Guest-Responsive Fluorescent 3D Microporous Metal−Organic Framework Derived from a Long-Lifetime Pyrene Core. *J. Am. Chem. Soc.* **2010**, *132*, 4119−4130.
(27) Dyadkin, V.; Pattison, P.; Dmitriev, V.; Chernyshov, D. A New Multipurpose Diffractometer PILATUS@SNBL. *J. Synchrotron Radiat.* **2016**, *23*, 825−829.
(28) Sheldrick, G. SHELXT − Integrated Space-group and Crystal-structure Determination. *Acta Crystallogr., Sect. A: Found. Adv.* **2015**, *71*, 3−8.
(29) Sheldrick, G. Crystal Structure Refinement with SHELXL. *Acta Crystallogr., Sect. C: Struct. Chem.* **2015**, *71*, 3−8.
(30) Dolomanov, O. V.; Bourhis, L. J.; Gildea, R. J.; Howard, J. A. K.; Puschmann, H. OLEX2: a Complete Structure Solution, Refinement and Analysis Program. *J. Appl. Crystallogr.* **2009**, *42*, 339−341.
(31) Blatov, V. A.; Shevchenko, A. P.; Proserpio, D. M. Applied Topological Analysis of Crystal Structures with the Program Package ToposPro. *Cryst. Growth Des.* **2014**, *14*, 3576−3586.
(32) Spek, A. PLATON SQUEEZE: a Tool for the Calculation of the Disordered Solvent Contribution to the Calculated Structure Factors. *Acta Crystallogr., Sect. C: Struct. Chem.* **2015**, *71*, 9−18.
(33) Rodríguez-Carvajal, J. Recent Advances in Magnetic Structure Determination by Neutron Powder Diffraction. *Phys. B* **1993**, *192*, 55−69.
(34) Soleimani Dorcheh, A.; Denysenko, D.; Volkmer, D.; Donner, W.; Hirscher, M. Noble Gases and Microporous Frameworks; from Interaction to Application. *Microporous Mesoporous Mater.* **2012**, *162*, 64−68.
(35) Xian, S.; Peng, J.; Zhang, Z.; Xia, Q.; Wang, H.; Li, Z. Highly Enhanced and Weakened Adsorption Properties of Two MOFs by Water Vapor for Separation of CO_2/CH_4 and CO_2/N_2 Binary Mixtures. *Chem. Eng. J.* **2015**, *270*, 385−392.
(36) Zhang, Y.; Xiao, H.; Zhou, X.; Wang, X.; Li, Z. Selective Adsorption Performances of UiO-67 for Separation of Light Hydrocarbons C1, C2, and C3. *Ind. Eng. Chem. Res.* **2017**, *56*, 8689−8696.
(37) Hamon, L.; Jolimaître, E.; Pirngruber, G. D. CO_2 and CH_4 Separation by Adsorption Using Cu-BTC Metal−Organic Framework. *Ind. Eng. Chem. Res.* **2010**, *49*, 7497−7503.
(38) Giannozzi, P.; Baroni, S.; Bonini, N.; Calandra, M.; Car, R.; Cavazzoni, C.; Ceresoli, D.; Chiarotti, G. L.; Cococcioni, M.; Dabo, I.; Dal Corso, A.; de Gironcoli, S.; Fabris, S.; Fratesi, G.; Gebauer, R.; Gerstmann, U.; Gougoussis, C.; Kokalj, A.; Lazzeri, M.; Martin-Samos, L.; Marzari, N.; Mauri, F.; Mazzarello, R.; Paolini, S.; Pasquarello, A.; Paulatto, L.; Sbraccia, C.; Scandolo, S.; Sclauzero, G.; Seitsonen, A. P.; Smogunov, A.; Umari, P.; Wentzcovitch, R. M. QUANTUM ESPRESSO: a Modular and Open-source Software Project for Quantum Simulations of Materials. *J. Phys.: Condens. Matter* **2009**, *21*, 395502.
(39) Perdew, J. P.; Burke, K.; Ernzerhof, M. Generalized Gradient Approximation Made Simple. *Phys. Rev. Lett.* **1996**, *77*, 3865−3868.

DOI: 10.1021/acsami.8b13362
ACS Appl. Mater. Interfaces 2018, 10, 36144−36156

(40) Grimme, S. Semiempirical GGA-type Density Functional Constructed with a Long-range Dispersion Correction. *J. Comput. Chem.* **2006**, *27*, 1787−1799.
(41) Blöchl, P. E. Projector Augmented-wave Method. *Phys. Rev. B: Condens. Matter Mater. Phys.* **1994**, *50*, 17953−17979.
(42) Dubbeldam, D.; Calero, S.; Ellis, D. E.; Snurr, R. Q. RASPA: Molecular Simulation Software for Adsorption and Diffusion in Flexible Nanoporous Materials. *Mol. Simul.* **2016**, *42*, 81−101.
(43) Martin, M. G.; Siepmann, J. I. Transferable Potentials for Phase Equilibria. 1. United-Atom Description of *n*-Alkanes. *J. Phys. Chem. B* **1998**, *102*, 2569−2577.
(44) Potoff, J. J.; Siepmann, J. I. Vapor−liquid Equilibria of Mixtures Containing Alkanes, Carbon Dioxide, and Nitrogen. *AIChE J.* **2001**, *47*, 1676−1682.
(45) Sarkisov, L. Molecular Simulation of Low Temperature Argon Adsorption in Several Models of IRMOF-1 with Defects and Structural Disorder. *Dalton Trans.* **2016**, *45*, 4203−4212.
(46) Vasudevan, V.; Mushrif, S. H. Force Field Parameters for N,N-Dimethylformamide (DMF) Revisited: Improved Prediction of Bulk Properties and Complete Miscibility in Water. *J. Mol. Liq.* **2015**, *206*, 338−342.
(47) Wu, X.; Huang, J.; Cai, W.; Jaroniec, M. Force Field for ZIF-8 Flexible Frameworks: Atomistic Simulation of Adsorption, Diffusion of Pure Gases as CH_4, H_2, CO_2 and N_2. *RSC Adv.* **2014**, *4*, 16503−16511.
(48) Campañá, C.; Mussard, B.; Woo, T. K. Electrostatic Potential Derived Atomic Charges for Periodic Systems Using a Modified Error Functional. *J. Chem. Theory Comput.* **2009**, *5*, 2866−2878.
(49) Vlugt, T. J. H.; García-Pérez, E.; Dubbeldam, D.; Ban, S.; Calero, S. Computing the Heat of Adsorption using Molecular Simulations: The Effect of Strong Coulombic Interactions. *J. Chem. Theory Comput.* **2008**, *4*, 1107−1118.
(50) Horn, H. W.; Swope, W. C.; Pitera, J. W.; Madura, J. D.; Dick, T. J.; Hura, G. L.; Head-Gordon, T. Development of an Improved Four-site Water Model for Biomolecular Simulations: TIP4P-Ew. *J. Chem. Phys.* **2004**, *120*, 9665−9678.
(51) Perger, W. F.; Criswell, J.; Civalleri, B.; Dovesi, R. Ab-initio Calculation of Elastic Constants of Crystalline Systems with the CRYSTAL Code. *Comput. Phys. Commun.* **2009**, *180*, 1753−1759.
(52) Golesorkhtabar, R.; Pavone, P.; Spitaler, J.; Puschnig, P.; Draxl, C. ElaStic: A Tool for Calculating Second-order Elastic Constants from First Principles. *Comput. Phys. Commun.* **2013**, *184*, 1861−1873.
(53) Gaillac, R.; Pullumbi, P.; Coudert, F.-X. ELATE: an Open-source Online Application for Analysis and Visualization of Elastic Tensors. *J. Phys.: Condens. Matter* **2016**, *28*, 275201.
(54) Kanoo, P.; Gurunatha, K. L.; Maji, T. K. Versatile Functionalities in MOFs Assembled from the Same Building Units: Interplay of Structural Flexibility, Rigidity and Regularity. *J. Mater. Chem.* **2010**, *20*, 1322−1331.
(55) Stylianou, K. C.; Bacsa, J.; Bradshaw, D.; Rosseinsky, M. J. A 3D Porous Metal Organic Framework Based on Infinite 1D Nickel(II) Chains with Rutile Topology Displaying Open Metal Sites. *Z. Anorg. Allg. Chem.* **2014**, *640*, 2123−2131.
(56) Zang, S.; Su, Y.; Duan, C.; Li, Y.; Zhu, H.; Meng, Q. Coexistence of Chiral Hydrophilic and Achiral Hydrophobic Channels in One Multi-helical-array Metal-organic Framework Incorporating Helical Water Cluster Chains. *Chem. Commun.* **2006**, 4997−4999.
(57) Ohmori, O.; Kawano, M.; Fujita, M. A Two-in-One Crystal: Uptake of Two Different Guests into Two Distinct Channels of a Biporous Coordination Network. *Angew. Chem.* **2005**, *117*, 1998−2000.
(58) Kawano, M.; Kawamichi, T.; Haneda, T.; Kojima, T.; Fujita, M. The Modular Synthesis of Functional Porous Coordination Networks. *J. Am. Chem. Soc.* **2007**, *129*, 15418−15419.
(59) Mohideen, M. I.; Xiao, B.; Wheatley, P. S.; McKinlay, A. C.; Li, Y.; Slawin, A. M.; Aldous, D. W.; Cessford, N. F.; Duren, T.; Zhao, X.; Gill, R.; Thomas, K. M.; Griffin, J. M.; Ashbrook, S. E.; Morris, R. E. Protecting Group and Switchable Pore-discriminating Adsorption Properties of a Hydrophilic-hydrophobic Metal-organic Framework. *Nat. Chem.* **2011**, *3*, 304−310.
(60) Jiao, J.; Dou, L.; Liu, H.; Chen, F.; Bai, D.; Feng, Y.; Xiong, S.; Chen, D. L.; He, Y. An Aminopyrimidine-functionalized Cage-based Metal−organic Framework Exhibiting Highly Selective Adsorption of C_2H_2 and CO_2 over CH_4. *Dalton Trans.* **2016**, *45*, 13373−13382.
(61) Chen, F.; Bai, D.; Wang, Y.; Jiang, D.; He, Y. A Family of ssa-type Copper-based MOFs Constructed from Unsymmetrical Diisophthalates: Synthesis, Characterization and Selective Gas Adsorption. *Mater. Chem. Front.* **2017**, *1*, 2283−2291.
(62) Ortiz, A. U.; Boutin, A.; Fuchs, A. H.; Coudert, F.-X. Metal−organic Frameworks with Wine-rack Motif: What Determines their Flexibility and Elastic Properties? *J. Chem. Phys.* **2013**, *138*, 174703.
(63) Nye, J. F. *Physical Properties of Crystals. Their Representation by Tensors and Matrices*; Oxford University Press: Oxford, 1957.
(64) Rogge, S. M. J.; Waroquier, M.; Van Speybroeck, V. Reliably Modeling the Mechanical Stability of Rigid and Flexible Metal−Organic Frameworks. *Acc. Chem. Res.* **2018**, *51*, 138−148.
(65) Witman, M.; Ling, S.; Jawahery, S.; Boyd, P. G.; Haranczyk, M.; Slater, B.; Smit, B. The Influence of Intrinsic Framework Flexibility on Adsorption in Nanoporous Materials. *J. Am. Chem. Soc.* **2017**, *139*, 5547−5557.
(66) The same desolvation process was recorded during the TGA experiment in a much broader temperature range, 305−520 K. The difference in the amount of sample probed (3.516 mg in the TGA experiment vs a small fraction of a 0.7 mm-thick capillary) could be the reason of this discrepancy.
(67) Serre, C.; Bourrelly, S.; Vimont, A.; Ramsahye, N. A.; Maurin, G.; Llewellyn, P. L.; Daturi, M.; Filinchuk, Y.; Leynaud, O.; Barnes, P.; Férey, G. An Explanation for the Very Large Breathing Effect of a Metal−Organic Framework during CO_2 Adsorption. *Adv. Mater.* **2007**, *19*, 2246−2251.
(68) Molecular volume of CH_4 was calculated from its density in liquid state at bp.
(69) A hydrophobic pore can accommodate 1.6 and a hydrophilic one, 2.7, with an average of 2.2 molecules of CO_2. Molecular volume of CO_2 was calculated analogously to that of CH_4.
(70) Serra-Crespo, P.; Ramos-Fernandez, E. V.; Gascon, J.; Kapteijn, F. Synthesis and Characterization of an Amino Functionalized MIL-101(Al): Separation and Catalytic Properties. *Chem. Mater.* **2011**, *23*, 2565−2572.
(71) Couck, S.; Gobechiya, E.; Kirschhock, C. E. A.; Serra-Crespo, P.; Juan-Alcañiz, J.; Joaristi, A. M.; Stavitski, E.; Gascon, J.; Kapteijn, F.; Baron, G. V.; Denayer, J. F. M. Adsorption and Separation of Light Gases on an Amino-Functionalized Metal−Organic Framework: An Adsorption and In Situ XRD Study. *ChemSusChem* **2012**, *5*, 740−750.
(72) Giménez-Marques, M.; Calvo Galve, N.; Palomino, M.; Valencia, S.; Rey, F.; Sastre, G.; Vitórica-Yrezábal, I. J.; Jiménez-Ruiz, M.; Rodríguez-Velamazán, J. A.; González, M. A.; Jordá, J. L.; Coronado, E.; Espallargas, G. M. Gas Confinement in Compartmentalized Coordination Polymers for Highly Selective Sorption. *Chem. Sci.* **2017**, *8*, 3109−3120.
(73) Bastin, L.; Bárcia, P. S.; Hurtado, E. J.; Silva, J. A. C.; Rodrigues, A. E.; Chen, B. A Microporous Metal−Organic Framework for Separation of CO_2/N_2 and CO_2/CH_4 by Fixed-Bed Adsorption. *J. Phys. Chem. C* **2008**, *112*, 1575−1581.

DOI: 10.1021/acsami.8b13362
ACS Appl. Mater. Interfaces 2018, 10, 36144−36156